Controlled joule-heating of suspended glassy carbon wires for localized chemical vapor deposition

Albert Cisquella-Serra [a, b], Manuel Gamero-Castaño [b, *], Laia Ferrer-Argemi [b], Jenna Wardini [b], Marc Madou [a, b, c]

[a] Materials and Manufacturing Technology, University of California, Irvine, CA, USA, 92617
[b] Mechanical and Aerospace Engineering, University of California, Irvine, CA, USA, 92617
[c] NANO - Sensors & Devices School of Engineering and Sciences Tecnológico de Monterrey, Mexico

A B S T R A C T

This paper demonstrates for the first time localized chemical vapor deposition of WO_{3-x} on a suspended glassy carbon wire. A process based on the photopatterning of an SU-8 scaffold, the near-field electro-spinning of an SU-8 fiber, and their pyrolysis yields a monolithic carbon structure featuring a glassy carbon wire of known diameter and length, suspended on a glassy carbon scaffold. The temperature required for the deposition of WO_{3-x} is generated by passing current through the wire, which causes Joule heating. The deposition starts in the midpoint of the wire, and extends to its ends as the current is increased. The thickness and length of the coating are functions of the imposed current. The evolution of the coating can be monitored in real time by measuring the voltage vs current characteristic of the wire. We have deposited WO_{3-x} coatings with thickness from 71 nm to 1.4 μm, in glassy carbon wires with diameters between 780 nm and 2.95 μm. The coatings are uniform and polycrystalline. The suspended glassy carbon wire is a generic platform for the deposition of many transition metal oxide (TMO) coatings, and opens the door to carbon-TMO structures for applications including catalysis and gas sensing.

© 2019 Elsevier Ltd. All rights reserved.

1. Introduction

Transition metal oxides (TMOs) have attracted considerable attention in applications such as gas sensing (enabled by their chemo-resistivity) and the catalysis of the oxygen reduction reaction (ORR) and the hydrogen evolution reaction (HER) [1,2]. Molecular hydrogen is a promising clean energy source, but the high cost of Pt-based catalysts handicaps large-scale applications. TMOs and other nonprecious-metal oxides could be economical alternatives to platinum, but are limited by either their poor electronic conductivity or their inadequate catalytic performance. Recent research suggests that the catalytic and sensing performances of TMOs can be improved when combined with carbon materials such as graphene [3,4], graphene oxide [5], carbon nanotubes (CNTs) [6], and pyrolytic carbon fibers. Zhang et al. [7] hybridized TiO_2 with graphite-like carbon layers to show that the semiconductor/graphite contact results in efficient separation of electron-hole pairs leading to higher photocatalytic activity under UV irradiation. Similarly, Woan et al. [8] demonstrated photocatalytic enhancement of TiO_2 by combining it with CNTs in a CNT-TiO_2 composite. Coating a suspended glassy carbon wire (GCW) with ZnO in a hydrothermal process led to lower limit of detection and higher sensitivity for NO_2 gas sensing than a single ZnO wire of the same dimensions [9]. Also carbon-SnO_2 hybrid structures have shown better electrochemical performance as anodes in lithium-ion batteries than pure SnO_2[[10—12]].

Nearly stoichiometric tungsten trioxide WO_{3-x} is a TMO suitable for electrochromic devices [13], gas sensing [14,15] and HER catalysis [16]. Furthermore, the insertion of this TMO in a carbon matrix enhances its catalytic performance[[17—20]]. For example Wu et al. [21] and Chen et al. [22] have synthetized composites of carbon fibers and tungsten oxide by preoxidizing and carbonizing a polymer matrix with embedded tungsten particle precursors. Both composites exhibit good HER performance, which the authors associate with the reduction of WO_3 by carbon during the carbonization step generating oxygen vacancies. However, the synthesis of these composites is difficult to control and reproduce. Here we introduce local chemical vapor deposition (LCVD) of TMOs on suspended carbon nanowires to learn how to design, fabricate and test novel TMO compositions on carbon fibers. The fabrication

* Corresponding author.
  E-mail address: mgameroc@uci.edu (M. Gamero-Castaño).

of these test structures includes the following steps: first, near-field electrospinning is used to suspend an SU-8 precursor fiber on a photopatterned SU-8 scaffold; pyrolysis of the SU-8 yields a monolithic carbon structure including a GCW of known diameter and length suspended on a glassy carbon (GC) scaffold with excellent ohmic contact. The well-defined geometry and transport properties of the GCW make it possible to accurately control its temperature profile by Joule heating, which in turn enables LCVD of TMOs.

Recent advances in the understanding of near-field electrospinning enables a better control of the dimensions of the suspended fibers, their precise placement, and also better control of the microstructure upon pyrolysis of the polymer wires [[23–26]]. Furthermore, the electrical and thermal conductivities of suspended GCWs have been characterized recently [27,28], making it possible to impose precise temperature profiles by Joule heating in these small test structures. This approach has been used in the past to change the microstructure of the suspended carbon wires [29], to weld fibers [30], and to fabricate nanogaps [31]. Glassy carbon is an ideal substrate for TMOs due to its low chemical reactivity and high thermal stability: glassy carbon is a low reactive carbon allotrope [32,33] which does not graphitize even at very high temperatures (e.g. 2500 °C) [34].

As a demonstration for the utility of our approach this article describes the local chemical vapor deposition of WO$_{3-x}$ on a suspended GCW by controlled Joule heating. We study the thickness of the coating as a function of LCVD deposition parameters, formulate a model to explain the coating process, and characterize the microstructure of the coating and the GCW. The well-known geometry and thermal properties of the suspended GCWs in our test structures constitute not only an ideal platform for testing the novel LCVD of TMOs, but are also useful for the production of a new class of gas sensors and can be scaled up for large catalysis applications (e.g. in fuel cells).

2. Experimental methods

Fig. 1 illustrates the fabrication steps for suspending a GCW on a glassy carbon scaffold, and depositing a layer of WO$_{3-x}$ on its surface by LCVD. Sections 2.1-2.3 describe the preparation of the sample, the annealing of the glassy carbon, the measurement of the GCW's temperature coefficient of resistance, and the deposition of the tungsten oxide.

2.1. Sample preparation

The scaffold, shown in Fig. S1 of the supplementary material, is lithographically patterned from SU-8 2025 on a silicon wafer with a 1 μm thick thermal oxide layer [27,28] Next, near-field electrospinning in contact-jet mode [24] is used to suspend an SU-8 2002 based polymer fiber on the desired section of the scaffold (Fig. 1a). Upon carbonization, the scaffold and suspended wire become a monolithic glassy carbon structure (Fig. 1b). The carbonization is carried out in a nitrogen atmosphere, using a heating ramp from room temperature to 300 °C of 4 °C/min, followed by a 1-h halt at 300 °C, a second heat ramp up to 900 °C of 10 °C/min, and a final halt of 1 h.

The space between the walls of the scaffold fixes the length of the GCW, which is accurately determined by photolithography. On the other hand, although progress has been made on the understanding of near-field electrospinning [24], the diameter of the deposited fiber cannot be accurately predetermined. In our set up we can obtain GCWs with diameters between 200 nm and 3 μm. Based on our experience we choose the polymer blend solution and operational parameters like the emitter voltage and the collector

speed to aim at a fiber diameter, but we do not have the control or reproducibility to accurately predetermine it. Furthermore the dimensions of the GCW are different from those of the deposited fiber due to the loss of non carbon atoms during the pyrolysis. The shrinkage of SU-8 photolithography structures during carbonization is well known and reported in the literature [35], and the change in dimensions can be predicted accurately. The dimensions of the suspended GCW are measured with a scanning electron microscope (SEM). We select GCWs with diameters near one micron to simplify their characterization.

The final glassy carbon structure on the SiO$_2$/Si substrate is mounted on a ceramic package and wire-bonded to the package's gold contact pins (Fig. 1d). To ensure good electrical connections with the gold pins a 500 nm thick layer of silver is deposited by e-beam evaporation on selected areas of the carbon structure (Fig. 1 c). The silver contact pads are deposited using a stencil copper mask fabricated with dry film lithography [36,37].

### 2.2. Annealing and measurement of the temperature coefficient of resistance

In order to perform localized chemical vapor deposition it is paramount to have a detailed knowledge of the temperature dependence of the resistivity of the GCW. Furthermore, this dependence must not change significantly as the GCW is heated both when measuring its temperature coefficient of resistance (TCR), and when performing LCVD. To avoid this unwanted variation of the TCR, caused by changes in the microstructure of the glassy carbon during heating [38], the GCW must be annealed to minimize those changes. The annealing is carried out for 6 h at 370 °C in a vacuum furnace, JANIS VPF-800 (Fig. 1e). Afterwards, we measure the electrical resistance R at different sample temperatures to compute the TCR of the GCW:

$$TCR = \frac{1}{R_0} \frac{dR}{dT} \tag{1}$$

where R_0 is the resistance at the reference temperature T_0, set at 295 K. The temperature dependence of the resistance $R(T)$ of the annealed GCW is characterized by measuring its current vs. voltage $I(V)$ response, using a 4-probe configuration in a current driven setup to avoid the influence of contact resistances [39,40]. The current, kept very low to avoid significant Joule heating, is injected with a Keithley 6221 current source and the resulting voltage difference across the GCW is measured with a precision Keysight 34465A multimeter. The sample is placed inside a vacuum chamber with a base temperature adjusted with a Lake Shore 330 temperature controller, and the temperature of the sample itself is measured with a platinum resistance temperature detector (RTD) attached to the sample with thermal paste. The $R(T)$ characteristic of the GCW in the temperature range of interest is nearly linear and has a negative slope, which is used to compute a single value of the TCR, equation (1), for the temperature range within which LCVD is performed.

2.3. Localized chemical vapor deposition

The sample is placed inside a custom glass reactor with four sealed electrical outlets and connected in a 4-probe configuration to avoid contact resistances (Fig. 1f). The reactor is divided into the actual CVD chamber (700 ml), and a pre-heating chamber (435 ml) containing the precursor solution and equipped with a flexible heater. The precursor consists of a solution of W(CO)$_6$ in Acetone/DMF (1:1) and is heated at reduced pressure, leading to its evaporation and transport to the CVD chamber. With the precursor
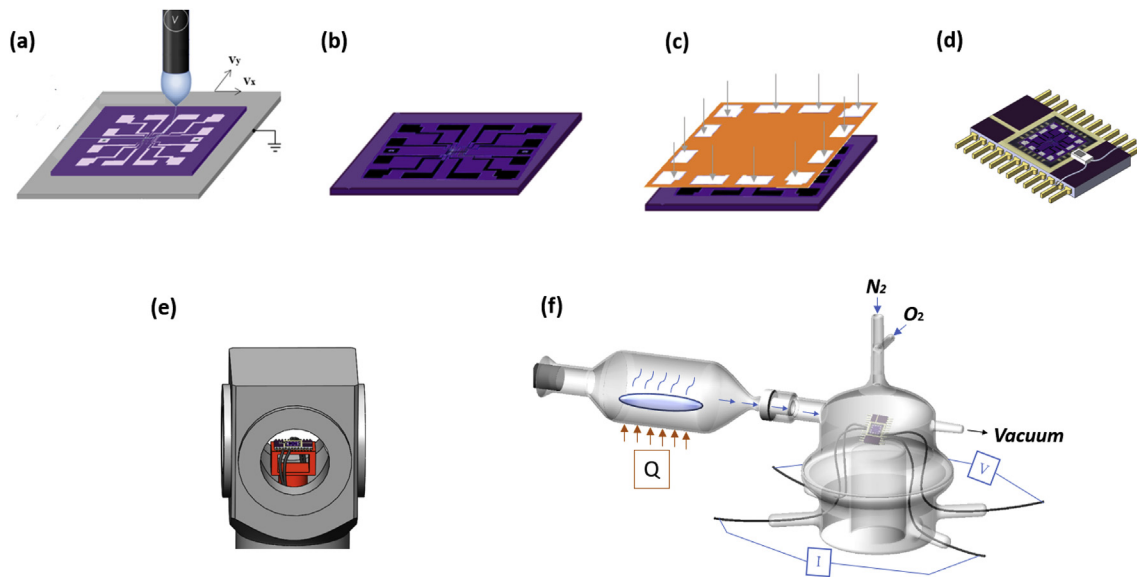
Fig. 1. Schematics of the microfabrication steps for performing LCVD on a suspended GCW: (a) deposition of a polymer fiber on a SU-8 patterned scaffold using near-field electrospinning; (b) pyrolyzed carbon monolithic structure with suspended GCWs; (c) e-beam deposition of silver pads for electrical contacts; (d) integration of the carbon monolith in a ceramic package including an RTD sensor; (e) annealing and measurement of the temperature coefficient of resistance of the GCW; (f) LCVD of WO_{3-x} on GCW. (A colour version of this figure can be viewed online.)

flowing into the CVD chamber, an increasing voltage (V_D) is applied to the sample using the 4-probe configuration (see Fig. S2 in supplementary material). The current and voltage at the terminals of the GCW are measured to compute its resistance and to estimate the average temperature increase with respect to T_0 using the *TCR* value:

$$\Delta T_{avg} \cong \frac{\Delta R}{TCR\, R_0} \tag{2}$$

2.4. Sample characterization

The geometry and the Raman spectra of the GCW and the WO_{3-x} coating are measured before and after LCVD with a FEI MAGELLAN 400 XHR scanning electron microscope (SEM) and an InVia Confocal Raman Microscope respectively. In addition, cross sections of the coated GCW are characterized with SEM-EDX and a JEOL 2800 transmission electron microscope (TEM) to obtain elemental maps and the atomic arrangement. The cross-sections are cut with a FEI Quanta 3D SEM/FIB (focused ion beam) following a procedure detailed in the supplementary material (see Fig. S3). The Raman spectroscopy is performed with a 532 nm excitation wavelength that is appropriate for both glassy carbon and WO_{3-x}, an 0.5% laser intensity and an exposure time of 5 s to avoid inducing microstructural changes in the sample [41].

3. Results and discussion

### 3.1. Process parameters required for LCVD of WO_{3-X}

We have deposited tungsten oxide coatings on suspended GCWs with thicknesses ranging from 70 nm to 1.4 μm. The LCVD process conditions studied include the CVD chamber pressure, the pre-chamber temperature, and the molarity of the precursor solution. Optimal conditions for the reactor include a chamber pressure of 60 mbar, a pre-chamber temperature of 90 °C, and a saturated $W(CO)_6$ solution. The decomposition and oxidation of $W(CO)_6$ to

WO_{3-x} at low pressures is well known [42,43]. Both molecular oxygen in the gas phase and the evaporated acetone [44] used as solvent for the precursor contribute to the oxidation of $W(CO)_6$ to WO_{3-x}. Coatings of WO_{3-x} were obtained at chamber pressures as high as 160 mbar as long as the O_2 partial pressure remains sufficiently low to avoid oxidizing the GCW during Joule heating. At chamber pressures above 160 mbar oxidation of the GCW leading to its thinning and even complete burning was observed (see Fig. S4 in supplementary material). Lower pre-chamber temperatures do not produce a sufficient vapor efflux from the solution, while higher pre-chamber temperatures result in evaporation rates too fast to enable controlled LCVD.

Fig. 2.a shows two suspended GCWs with different lengths and diameters, before and after LCVD. The formation of the WO_{3-x} coating is restricted to the length of the GCW and does not extend to either the glassy carbon scaffold or the SiO_2 surface of the substrate. Note also the different thicknesses of the coatings. Fig. 2.b shows how fibers in the same chip can be coated with different thicknesses, while other fibers remain uncoated. The scaffold connections and the resulting independent control of the current injected through each fiber make this possible.

3.2. WO_{3-X} coating formation and temperature profiles

In Fig. 3 we show the voltage vs. current characteristics of several GCWs labeled A to F, during the deposition of WO_{3-x}, as well as SEM images of the final state of the GCWs. The $V(I)$ curves reflect the LCVD process path, and also depend on the geometry of the glassy carbon wire. The different $V(I)$ curves are chosen to illustrate the stages of the coating process. In the actual experiments we recorded and analyzed these paths to understand how the deposition takes place. Note also that the control variable in the experiments is the voltage V_D driving the 4-point configuration (see Fig. S2 in supplementary material), while the resulting values of V and I plotted in Fig. 3 are defined at the terminals of the GCW of interest (i.e. a section of the glassy carbon wire limited by two consecutive walls of the scaffold). The diameter, the length, the resistance at room temperature and the *TCR* of each GCW are given
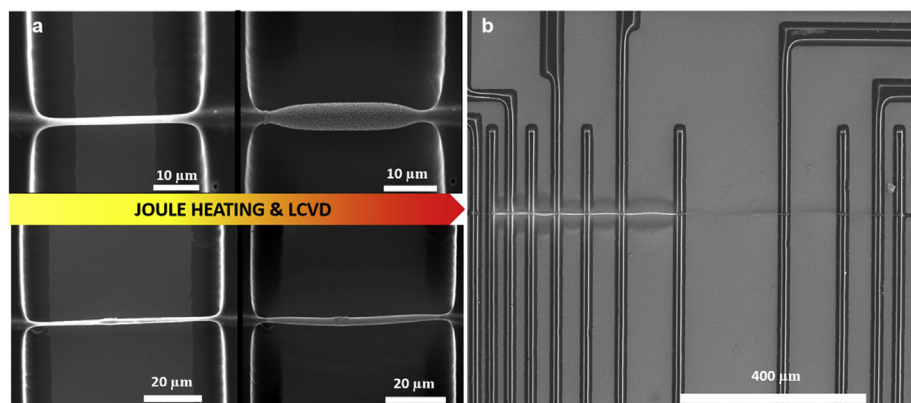
Fig. 2. a) SEM pictures of suspended GCWs before and after the LCVD process; b) overview of multiple fibers suspended from scaffolds, illustrating how they can be locally coated (bright fibers) or left uncoated (darker fibers) without contaminating the carbon scaffold. (A colour version of this figure can be viewed online.)
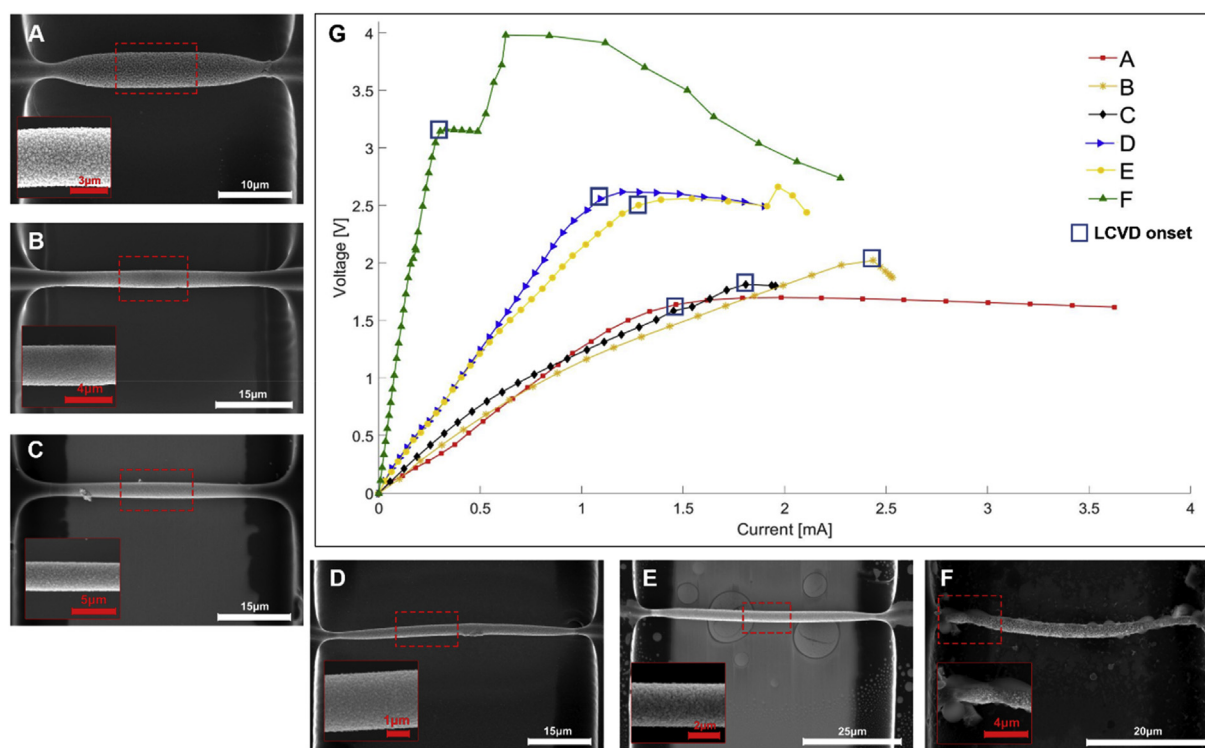
Fig. 3. SEM images of GCWs at different coating stages (A–F), together with the V(I) characteristics used for each coating (G). (A colour version of this figure can be viewed online.)

Table 1
Values of the diameter, length, resistance at room temperature R_0 and TCR of different GCWs before WO_{3-x} deposition, together with the coating thickness, the ratio I/I_{on} between the currents at the end and the start of the deposition, and the resistance at room temperature after deposition.

	GCW A	GCW B	GCW C	GCW D	GCW E	GCW F
Diameter (μm)	1.27	2.95	2.78	1.83	1.66	0.78
Length (μm)	31.37	46.16	50.16	60.33	63.75	52.382
$R_0(\Omega)$	1273	1387	1718	3422	3475	13472.57
$TCR\ (K^{-1})$	0.0013	0.00052	0.00055	0.00094	0.00106	0.00053
Coating thickness (μm)	1.42	0.07	0.12	0.29	0.48	–
Current ratio I/I_{on}	2.48	1.04	1.17	1.74	1.76	–
$R_{after}(\Omega)$	4697	2192	–	5442	–	–

in Table 1. The $V(I)$ curve for fiber A illustrates a typical LCVD experiment: at first, an increase in I results in an almost linear increase of V, with only a slight deviation from linearity due to Joule heating and the negative value of the TCR. The quasi linear $V(I)$

trend then transitions into a plateau around the point {1.46 mA, 1.64 V}. Joule heating at this point raises the temperature at the middle of the GCW to the value required to initiate the deposition of WO_{3-x}. The flattening of the $V(I)$ curve indicates that the

deposition of WO_{3-x} decreases the overall resistance of the suspended wire. Since the deposition is progressing from the middle of the GCW towards its contacts with the scaffold, this indicates that the equivalent resistivity of the coated section must be lower than the resistivity of the uncoated GCW. The SEM image of the final state of the sample shows a thick coating covering fiber A, which is uniform in diameter except for a progressive thinning near the contacts. The $V(I)$ curve for fiber B is similar up to the start of the plateau, at which point the voltage V_D driving the 4-point configuration is kept constant. This results in a decrease of the voltage V across the fiber, and a slight increase of I. The SEM image of the sample B shows a very thin coating only in the middle of the fiber. The $V(I)$ curve for fiber C is carried out slightly differently: once the plateau is reached, instead of fixing V_D we increase its value by 1.1 V. The start of the plateau is discernible in this case, resulting in a thin coating slightly thicker than for fiber B, but which neither extends to the contacts with the scaffold. The $V(I)$ curve for fiber D is similar to that of fiber A (initial quasi linear ramp followed by and extended plateau), and produces a relatively thick coating that extends to near the contacts. The resistance at room temperature of fiber D is significantly higher than those of fibers A, B and C, the slope of its $V(I)$ curve is accordingly larger, and the increased Joule dissipation ($\sim RI^2$) requires a lower current to reach the critical temperature needed for CVD. The $V(I)$ curve for fiber E extends to form a broad plateau, but at the current value of 1.92 mA it starts increasing to later decrease again, at which point the experiment was terminated. The SEM image of this sample reveals a thick coating that also covers the contacts with the scaffold. Finally, the $V(I)$ curve for fiber F (which has the highest R_0) features the typical initial quasilinear ramp, an extended plateau, a second linear increase, and a final erratic decrease. The SEM image of this fiber shows a thick coating extending all the way to the contacts with the scaffold, and the disappearance of the coating at several points as locally the temperature becomes high enough to melt the coating. The end of the plateau coincides with the coating of the fiber reaching the contacts, at which point the coated fiber behaves like a single resistor (V and I are proportional with a significant positive slope).

Since the temperature profile is a critical parameter in the LCVD of WO_{3-x}, knowledge of the temperature profile along the suspended fiber is needed to understand the deposition process including the $V(I)$ curves in Fig. 3. The temperature profile $T(x)$ can be estimated with the following one-dimensional equation and boundary conditions:

$$\frac{d^2T}{dx^2} + \frac{I^2 R_o'}{\kappa A}[1 + TCR(T - T_o)] = 0 \tag{3}$$

$$\left.\frac{dT}{dx}\right|_{x=0} = 0, T(L/2) = T_o$$

In this model the GCW has a constant cross section A, length L, and a resistance per unit length R_o' at room temperature T_o. I is the electrical current flowing through the fiber. For simplicity we assume constant thermal conductivity κ and TCR; see Ferrer-Argemi et al. [27] for a more accurate GCW thermal model that retains the temperature dependence of these parameters. Equation (3) represents the balance between heat conduction and Joule heating: convection is negligible at the reduced pressure of the reactor, while radiation can be neglected at the temperatures typical of the LCVD process. We set the origin of the axial coordinate at the middle of the GCW (symmetry requires a zero heat flux at this point), while its ends remain at room temperature (in the actual configuration the scaffold acts as a thermal bath). The analysis is simplified by rewriting these equations in dimensionless form

using the dimensionless temperature $\theta = (T - T_o)/T_o$ and the dimensionless coordinate $\tilde{x} = x/L$:

$$\frac{d^2\theta}{d\tilde{x}^2} + \Pi^2(1 + T_o TCR\,\theta) = 0 \tag{4}$$

$$\left.\frac{d\theta}{d\tilde{x}}\right|_{\tilde{x}=0} = 0, \theta(1/2) = 0$$

These equations show that the $\theta(\tilde{x})$ profile is just a function of the dimensionless number $\Pi = \sqrt{\frac{I^2 R_o' L^2}{\kappa A T_o}}$ and the product $T_o TCR$. The solution is

$$\theta(\tilde{x}) = \frac{1 + e^{\sqrt{-T_o TCR}\Pi} - e^{\frac{1}{2}(1-2x)\sqrt{-T_o TCR}\Pi} - e^{\frac{1}{2}(1+2x)\sqrt{-T_o TCR}\Pi}}{\left(1 + e^{\sqrt{-T_o TCR}\Pi}\right)(-T_o TCR)} \tag{5}$$

which has the following maximum at the middle of the GCW:

$$\theta_{max} = \frac{\left(-1 + e^{\frac{1}{2}\sqrt{-T_o TCR}\Pi}\right)^2}{\left(1 + e^{\sqrt{-T_o TCR}\Pi}\right)(-T_o TCR)} \tag{6}$$

In Fig. 4 we illustrate three temperature profiles obtained from this model. Curve 1 is the solution for $\Pi = 5.68$ and $T_o TCR = -0.387$, i.e. for fiber A in Table 1 at the onset of LCVD, $I = 1.46\,mA$; we use $\kappa = 7$ to take into account the elevated temperature of the GCW. The profile is monotonic and has a maximum at its center with a value of $\theta_{max} = 1.73$ or equivalently $T_{max} = 539^o C$, which is within the range of the deposition temperatures for WO_{3-x} [42,43]. If this maximum temperature is near the critical value triggering chemical vapor deposition, only a small section of the GCW around the midpoint will be coated with WO_{3-x}. Furthermore, from the description of Fig. 3, we know that at the deposition temperature the central section of the GCW coated with WO_{3-x} has a lower linear resistance than the uncoated fiber. The lower resistivity of the coated section reduces Joule heating in this area ($\sim I^2 R$), lowering
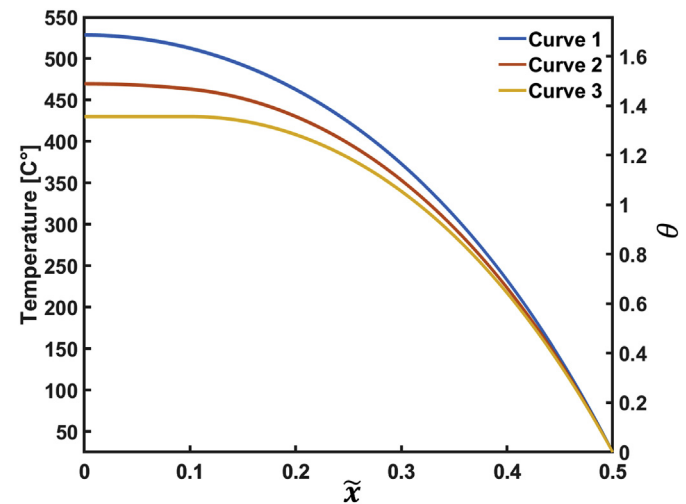
Fig. 4. Temperature profiles along the GCW, equation (7), for $\Pi = 5.68$ and $T_o TCR = -0.387$, and different lengths of the coating: Curve 1 is for an uncoated GCW; Curve 2 is for a GCW with a coated section having a resistivity one third of the original GCW and extending 20% of the GCW length; Curve 3 is for a coated section with negligible resistivity and extending 20%. (A colour version of this figure can be viewed online.)

the temperature profile at fixed Π and quenching the deposition. This scenario is readily verified by modifying Equation (4) to account for the change in the linear resistance between the coated and non-coated sections:

$$\frac{d^2\theta}{d\tilde{x}^2} + \Pi^2 \frac{R_o'(\tilde{x})}{R_o'}(1 + T_o TCR(\tilde{x})\theta) = 0 \qquad (7)$$

Curve 2 in Fig. 4 is the solution of this equation for $\Pi = 5.68$, $T_o TCR = -0.387$ and a coated section with one third of the resistivity of the original GCW extending over 20% of the GCW length. This temperature profile is always lower than Curve 1, the temperature profile for the uncoated GCW heated up by the same current. Curve 2 also has a maximum temperature at the center with values $\theta_{max} = 1.53$ and $T_{max} = 481^oC$. Curve 3 is for a coating with the same length in the limiting case of zero resistivity, and $\Pi = 5.68$, $T_o TCR = -0.387$. The temperature profile is flat in the coated region because of the absence of Joule heating in this section, and is lower than both Curves 1 and 2. Given that the deposition of WO_{3-x} quenches the LCVD at constant Π (i.e. at constant current for a fixed GCW geometry), extending the coating towards the ends of the GCW requires a continuous increase of Π or, equivalently, of the current injected through the fiber. This model also explains the plateaus in the $V(I)$ curves shown in Fig. 3: when the resistivity of the coated section is much smaller than that of the original GCW, the temperature profile in the coated region is flat and decreases monotonically in the non-coated section (see Fig. 4, Curve 3). The profile in the non-coated section during further deposition is then the solution of Equation (4) with the origin of the coordinates shifted to the interface between coated and non-coated sections, and with the length of the non-coated section L_{nc} now playing the role of characteristic length, $\Pi = \sqrt{\frac{I^2 R_o L_{nc}^2}{\kappa A T_o}}$. When the current injected through the GCW is increased slowly the interface between the coated and non-coated sections shifts towards the ends of the GCW at constant maximum temperature (due to the self-quenching character of the deposition), and therefore at constant Π, Eq. (6). The voltage V across the GCW is the voltage drop along the non-coated section (the resistance of the coated section is comparatively small), and therefore proportional to $L_{nc}I$. Since Π is constant during deposition, $L_{nc}I$ and V must be constant as well, i.e. the deposition proceeds at constant voltage difference across the GCW.

The coating thickness increases with the ratio between the current passing through the GCW and the onset value I_{on} needed to start the deposition. For example, the ratio $D_c/D_o = 3.24$ between the diameters of the coated (D_c) and uncoated fiber (D_o) in Fig. 3A is obtained with a current ratio $I/I_{on} = 2.48$. The same values for Fig. 3B, 3C, 3D and 3E are $D_c/D_o = \{1.04, 1.09, 1.32, 1.58\}$, and $I/I_{on} = \{1.04, 1.17, 1.74, 1.76\}$. We show in Fig. 5 the profiles of the coated fibers A and B. When the fiber is coated up to the contacts with the scaffold (e.g. fiber A), the thickness of the coating is uniform along most of its length, and decreases smoothly near the contacts. Furthermore, at very high values of I/I_{on} the coating may melt, and/or the scaffold area near the fiber may become hot enough to induce LCVD on the scaffold (see Fig. S5 in supplementary information).

The foregoing experiments and analysis demonstrate that there is a one-to-one correspondence between the current passed through the GCW and the state of the coating for a given GCW and conditions in the CVD chamber. Therefore the current can be used to control the deposition. However, at this point we cannot determine a priori the value of the current that will produce a prescribed coating state for any given GCW. To do this we would need a better deposition model. An alternative for producing a prescribed coating would be to monitor the coating and actuate the current until the desired coating is obtained.
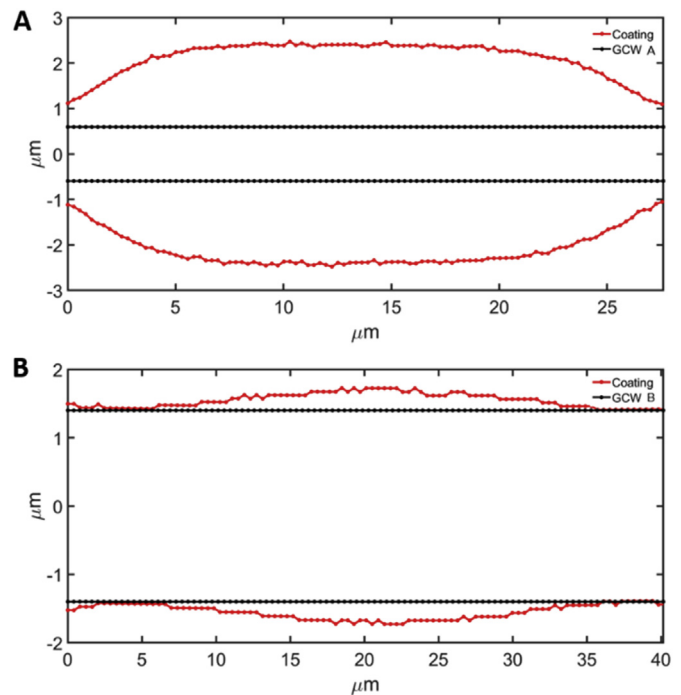

Fig. 5. Profiles of the A and B GCWs (black), together with their profiles after deposition of WO_{3-x} (red). (A colour version of this figure can be viewed online.)

3.3. Microscopy characterization of WO_{3-x} coatings and GCWs

Fig. 6a and 6.b show SEM pictures of the surfaces of two WO_{3-x} coatings, formed by agglomerated nanoparticles of uniform size. Fig. 6c-6.f shows the cross-section of a GCW with a coating thickness of 1.05 μm and EDX elemental mappings. The SEM image 6.c shows a clear distinction between the glassy carbon core and the surrounding WO_{3-x} coating. The elemental mappings show a core of carbon matching the section of the GCW, while the surrounding area of the coating is composed of oxygen and tungsten proving the coating to be in the form of a tungsten oxide. Table 2 shows the concentrations (in weight % and atomic %) of carbon, oxygen and tungsten in the cross section, estimated via EDX quantitative analysis. Although the uncertainty of this technique for light elements like carbon and oxygen is generally high, the low values of the statistical error σ supports the validity of the concentrations. The global W−O atomic ratio in the section is 1:2.6, i.e. slightly below the 1:3 stoichiometric value of WO_3. This oxygen deficiency could be due to oxygen vacancies, and/or the formation of a thin layer of WC surrounding the carbon core which is observed in the TEM characterization described below. Fig. S6, Table S1 and the accompanying text in the supplementary material provide additional details of the quantitative analysis.

Fig. 6g and 6.h shows Raman spectra of a non-coated GCW and a coated one respectively. The non-coated GCW shows the characteristic spectrum of glassy carbon with two Gaussian peaks associated with small graphite crystallites without long range translation symmetry (D band, 1300 - 1400 cm^{-1}), and in plane displacement of the carbons in the hexagonal sheets (G band, 1560-1610 cm^{-1}); the measured intensity ratio $I_D/I_G = 1.04$ is typical of glassy carbon [28]. The spectrum for the coated GCW shows several characteristic WO_{3-x} peaks: the peaks at 803.3 and 704.5 cm^{-1} correspond to the O−W−O stretching modes, while the 327.5 and 263.5 cm^{-1} peaks correspond to the O−W−O bending modes [45]; the two peaks at 185.2 and 128.9 cm^{-1} correspond to the lattice modes [47]. The spectrum also features a lower peak at 981.3 cm^{-1}
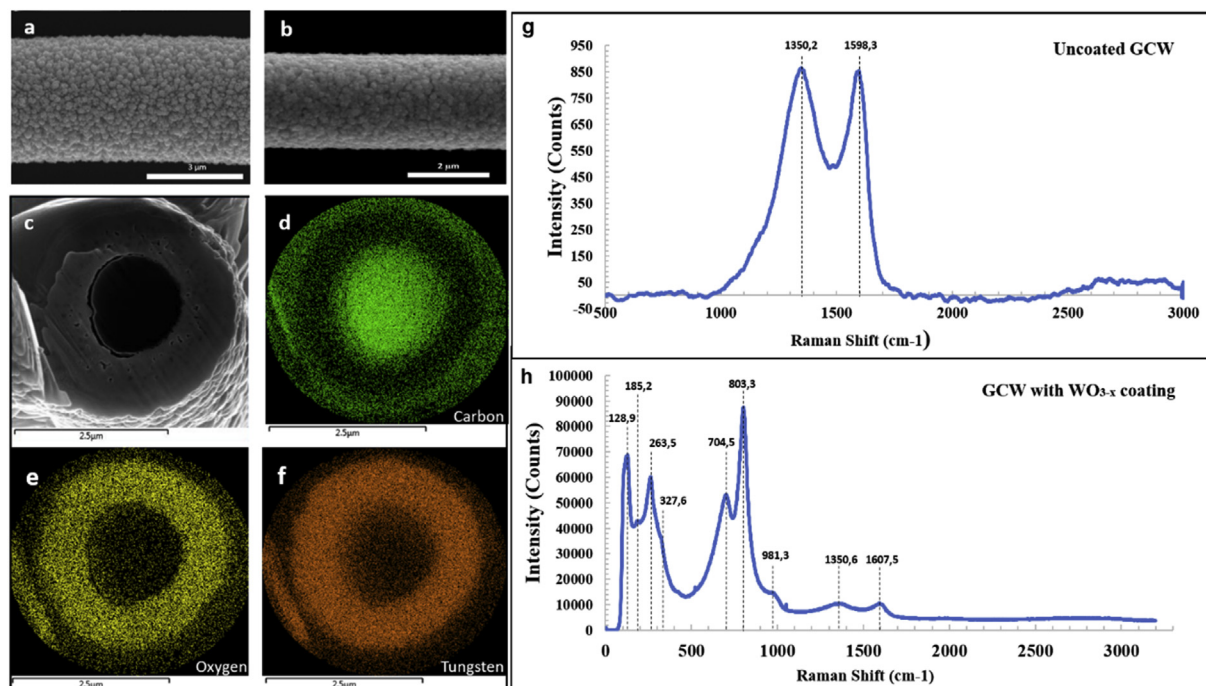
Fig. 6. a & b) SEM images of the surface microstructure of typical coatings; c) SEM image of the cross section of a coated GCW; d-f) EDX elemental mappings of carbon, oxygen and tungsten of the cross section in c); g) Raman spectrum of an uncoated GCW; h) Raman spectrum of a GCW coated with WO_{3-x}. (A colour version of this figure can be viewed online.)

Table 2
EDX quantitative analysis of the section shown in Fig. 6 c, including concentrations of carbon, oxygen and tungsten and the statistical error σ of the estimation.

| Element	Line type	Apparent concentr.	Weight %	σ (Weight %)	Atomic %
Carbon	K series	0.61	27.89	0.18	66.82
Oxygen	K series	0.81	13.33	0.12	23.98
Tungsten	M series	1.95	58.79	0.21	9.2

corresponding to the stretching mode of the W=O bond typical of hydrated tungsten trioxide crystals, and which has also been observed in samples calcinated between 400 and 500 °C [46]. The lower peaks at 1350.6 and 1607.5 cm^{-1} are produced by the GCW substrate.

The TEM data presented in Fig. 7 reveals the detailed microstructure of the cross section of a coated GCW, taken from a point near the midsection of the wire (see Fig. S3 in supplementary material for details on sample preparation). The bright-field TEM image in Fig. 7.a shows that the coating has a polycrystalline structure with an increasing crystallite size and density approaching the outer layer of the coating. The uniform contrast of the wire core indicates that it likely has the expected amorphous structure, which is confirmed in Fig. 7.f with high-resolution TEM (HR-TEM) and selected-area electron diffraction (SAED). The transition from the amorphous GC to the crystalline WO_{3-x} is captured in Fig. 7.b with a high magnification view of the region outlined in Fig. 7.a. The approximately 50 nm GCW-WO_{3-x} interface displays nanoscale crystallites which become larger and more interconnected through the thickness of the interface away from the core. The dispersed bright regions in the coating indicate the presence of porosity. The Scanning TEM-secondary electron image (STEM-SEI) of the coating in Fig. 7.c is used to confirm that these regions are in fact voids rather than additional GC regions. HR-TEM images of the outer portion of the coating, the interface, and the amorphous GC are presented in Fig. 7d-7.f respectively. The SAED patterns displayed in the insets are taken from identically sized areas centered on the

region presented in the corresponding HR-TEM image. The HR-TEM images of the coating regions in Fig. 7d and 7.e shows lattice fringes and their corresponding SAED spot patterns confirm the polycrystalline nature of these regions. The d-spacings obtained from the SAED pattern in Fig. 7.d for the bulk of the coating correlate well with the monoclinic phase of WO_3 (see Fig. S7 and Table S2 in the supplementary material). Some d-spacings seem to be associated with the presence of $WO_{2.72}$ (JCPDS Card No. 732177) [47], and a few outliers may imply the presence of a third phase. Finally, HR-TEM of the GC core in Fig. 7.f reveals the characteristic tight fragments of curved carbon sheets formed by hexagonal and non-hexagonal carbon rings [32,33], and the diffuse intensity of the SAED pattern also confirms the amorphous structure of this region.

Fig. 8 includes HR-TEM images of the bulk of the coating and the interface with the GCW, together with the measurement of lattice spacings. The measured spacing value of 0.38 nm and of 0.37 nm in the bulk of the coating correspond to WO_{3-x} in the (020) plane (JCPDS Card No.830951) [47]. Furthermore, these lattice spacings remain constant everywhere in Fig. 8a. In the interface, Fig. 8b, although the atomic arrangement is crystalline everywhere except for the GC amorphous phase in the bottom right corner, we measure a variety of lattice spacings, as illustrated by the value of 0.44 nm in Fig. 8c. We associate this non uniformity to a variation of the stoichiometry of the tungsten oxide, with a decrease in the concentration of oxygen closer to the GC core. Finally, closer to the amorphous GC core but still in the crystalline phase, Fig. 8d, we observe a layer with a lattice spacing of 0.28 nm, a value reported
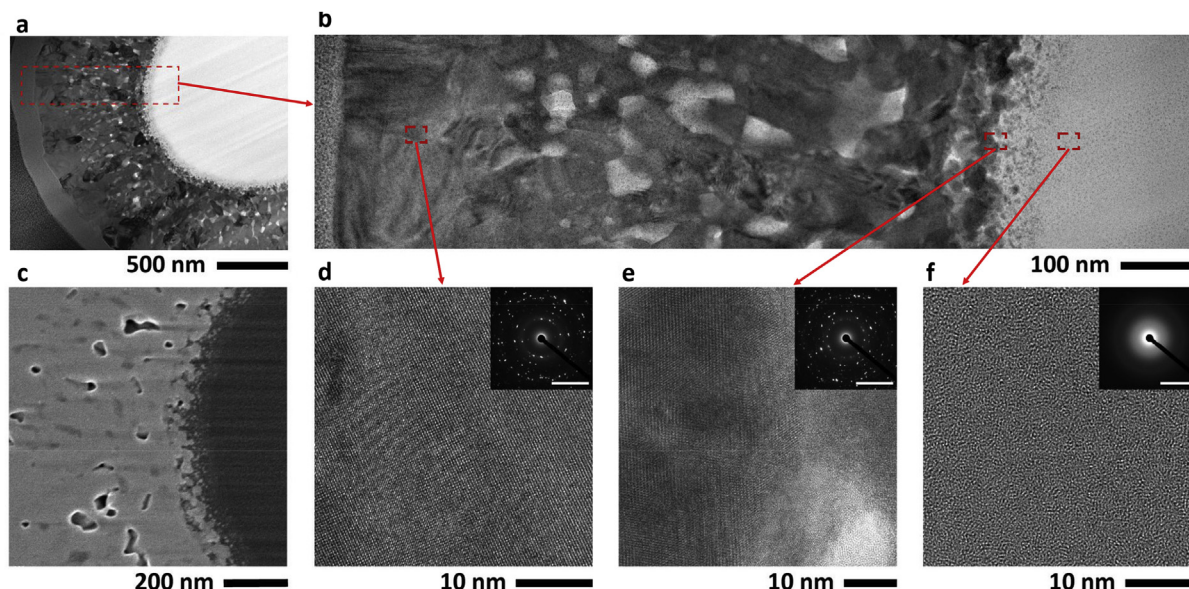
Fig. 7. a) bright-field TEM image showing the polycrystalline tungsten oxide coating surrounding the amorphous carbon wire; b) magnified image of the area outlined in a); c) dark-field TEM image of the coating, interface and GCW showing isolated voids in the coating; d-f) HR-TEM images of the bulk of the coating, interface and amorphous GCW core. (A colour version of this figure can be viewed online.)
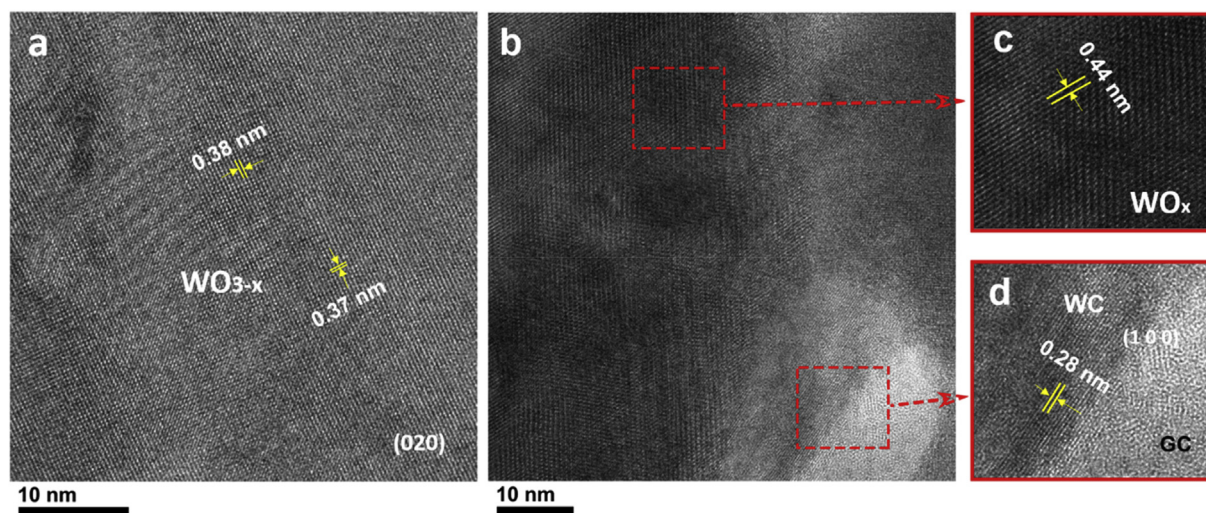
Fig. 8. HR-TEM images with measurements of lattice spacings. a) Bulk of the WO_{3-x} phase; b) interface between coating and GCW; c) detail of the crystalline phase in the interface, away from the GCW; d) detail of the crystalline phase in the interface, near the GCW. (A colour version of this figure can be viewed online.)

for WC (JCPDS Card No.510939) [48]. The reduction of WO_{3-x} to WC is thermodynamically favored in the presence of carbon at low oxygen pressures [49,50] We think that as the coating thickness increases, the access of oxidizing agents to the coating-GCW interface decreases, promoting the reduction of WO_{3-x} by carbon from the GCW. This reduction of the oxide suggests that the stoichiometry of the WO_{3-x} coating can be controlled in our system by annealing the GCW and its coating in either vacuum or an oxygen-rich atmosphere.

4. Conclusion

We have developed a novel GC/TMO microstructure consisting of a suspended GCW coated with WO_{3-x}, together with its microfabrication process. The coating is deposited by LCVD, activated by a temperature profile induced by Joule heating. The deposition of WO_{3-x} starts at the midpoint of the GCW, coinciding with the maximum of the temperature profile. Extending the coating towards the ends of the GCW requires increasing the current, while the voltage across the GCW remains constant. A thermal model shows that the constancy of the voltage at increasing current is due to the lower resistivity of the coated section at the deposition temperature; furthermore, the maximum of the temperature profile remains constant and shifts towards the ends of the GCW as the coating proceeds. Ultimately the length and thickness of the coating can be adjusted by imposing the current through the GCW and monitoring its voltage. We have demonstrated WO_{3-x} coatings with thickness ranging from 71 nm to 1.4 μm in glassy carbon wires with diameters between 780 nm and 2.95 μm. The stoichiometry of the coating (in terms of oxygen concentration) may be controlled

by a post-annealing treatment in either an oxygen rich atmosphere or vacuum, favoring the oxidation of WO_{3-x} or its reduction by the carbon respectively.

The suspended GCW described in this article is a generic platform that can be used for the deposition of many TMO coatings simply by changing the CVD precursor. The carbon scaffold/electrodes allow for the monitoring of thermal and electrical properties of the suspended fiber during deposition, making the structure a generic platform for materials characterization. The microfabrication process is scalable and can be used to make large scale catalysts. Finally, the results obtained in this study advance our understanding of LCVD on microstructures and open the door to a plethora of GCW-based sensors for different applications.

Acknowledgments

Appendix A. Supplementary data

Supplementary data to this article can be found online at https://doi.org/10.1016/j.carbon.2019.09.069.

References

[1] C. Wang, L. Yin, L. Zhang, D. Xiang, R. Gao, Metal oxide gas sensors: sensitivity and influencing factors, Sensors 10 (3) (2010) 2088—2106.

[2] G. Korotcenkov, "Metal oxides for solid-state gas sensors : what determines our choice ? Mater. Sci. Eng. B 139 (2007) 1—23.

[3] L. Zeng, T.S. Zhao, L. An, G. Zhao, X.H. Yan, C.Y. Jung, Graphene-supported platinum catalyst prepared with ionomer as surfactant for anion exchange membrane fuel cells, J. Power Sources 275 (2015) 506—515.

[4] X. Liu, W. Liu, M. Ko, M. Park, M.G. Kim, P. Oh, S. Chae, S. Park, A. Casimir, G. Wu, J. Cho, Metal (Ni, Co)-Metal oxides/graphene nanocomposites as multifunctional electrocatalysts, Adv. Funct. Mater. 25 (36) (2015) 5799—5808.

[5] Q. Li, P. Xu, B. Zhang, H. Tsai, J. Wang, H.L. Wang, G. Wu, One-step synthesis of Mn3O4/reduced graphene oxide nanocomposites for oxygen reduction in nonaqueous Li-O2 batteries, Chem. Commun. 49 (92) (2013) 10838—10840.

[6] C. Balázsi, K. Sedlácková, E. Llobet, R. Ionescu, Novel hexagonal WO3 nanopowder with metal decorated carbon nanotubes as NO2 gas sensor, Sens. Actuators B Chem. 133 (1) (2008) 151—155.

[7] L.W. Zhang, H.B. Fu, Y.F. Zhu, Efficient TiO2 photocatalysts from surface hybridization of TiO2 particles with graphite-like carbon, Adv. Funct. Mater. 18 (15) (2008) 2180—2189.

[8] K. Woan, G. Pyrgiotakis, W. Sigmund, Photocatalytic carbon-nanotube-TiO2 composites, Adv. Mater. 21 (21) (2009) 2233—2239.

[9] Y. Lim, S. Kim, Y.M. Kwon, J.M. Baik, H. Shin, A highly sensitive gas-sensing platform based on a metal-oxide nanowire forest grown on a suspended carbon nanowire fabricated at a wafer level, Sens. Actuators B Chem. 260 (2018) 55—62.

[10] P. Wu, N. Du, H. Zhang, J. Yu, Y. Qi, D. Yang, Carbon-coated SnO2 nanotubes: template-engaged synthesis and their application in lithium-ion batteries, Nanoscale 3 (2) (2011) 746—750.

[11] J. Kong, Z. Liu, Z. Yang, H.R. Tan, S. Xiong, S.Y. Wong, X. Li, X. Lu, Carbon/SnO 2/carbon core/shell/shell hybrid nanofibers: tailored nanostructure for the anode of lithium ion batteries with high reversibility and rate capacity, Nanoscale 4 (2) (2012) 525—530.

[12] B. Zhang, Y. Yu, Z. Huang, Y.B. He, D. Jang, W.S. Yoon, Y.W. Mai, F. Kang, J.K. Kim, Exceptional electrochemical performance of freestanding electrospun carbon nanofiber anodes containing ultrafine SnOx particles, Energy Environ. Sci. 5 (12) (2012) 9895—9902.

[13] S.K. Deb, Opportunities and challenges in science and technology of WO3 for electrochromic and related applications, Sol. Energy Mater. Sol. Cells 92 (2) (2008) 245—258.

[14] A. Staerz, U. Weimar, N. Barsan, "Understanding the potential of WO₃ based sensors for breath analysis, Sensors 16 (11) (2016) 1815.

[15] X.L. Li, T.J. Lou, X.M. Sun, Y.D. Li, Highly sensitive WO 3 hollow-sphere gas sensors, Inorg. Chem. 43 (17) (2004) 5442—5449.

[16] M.M. Mohamed, T.M. Salama, M.A. Hegazy, R.M. Abou Shahba, S.H. Mohamed, Synthesis of hexagonal WO 3 nanocrystals with various morphologies and their enhanced electrocatalytic activities toward hydrogen evolution, Int. J.

[17] Hydrogen Energy 44 (10) (2019) 4724—4736.

[17] L. Wang, X. Xu, Z. Feng, L. Bian, Y. Wang, WO3-x based composite material with chitosan derived nitrogen doped mesoporous carbon as matrix for oxygen vacancy induced organic pollutants catalytic reduction and IR driven H2 production, J. Solid State Chem. 266 (2018) 23—30.

[18] M.B. Tahir, G. Nabi, A. Hassan, T. Iqbal, H. Kiran, A. Majid, Morphology tailored synthesis of C-WO3 nanostructures and its photocatalytic application, J. Inorg. Organomet. Polym. Mater. 28 (3) (2018) 738—745.

[19] C. Wang, Y. Zhao, L. Zhou, Y. Liu, W. Zhang, Z. Zhao, W.N. Hozzein, H.M.S. Alharbi, W. Li, D. Zhao, Mesoporous carbon matrix confinement synthesis of ultrasmall WO3 nanocrystals for lithium ion batteries, J. Mater. Chem. 6 (43) (2018) 21550—21557.

[20] M. Bilal Tahir, G. Nabi, M. Rafique, N.R. Khalid, Role of fullerene to improve the WO3 performance for photocatalytic applications and hydrogen evolution, Int. J. Energy Res. 42 (15) (2018) 4783—4789.

[21] R. Wu, J. Zhang, Y. Shi, D. Liu, B. Zhang, Metallic WO2-carbon mesoporous nanowires as highly efficient electrocatalysts for hydrogen evolution reaction, J. Am. Chem. Soc. 137 (22) (2015) 6983—6986.

[22] J. Chen, D. Yu, W. Liao, M. Zheng, L. Xiao, H. Zhu, M. Zhang, M. Du, J. Yao, WO3-x nanoplates grown on carbon nanofibers for an efficient electrocatalytic hydrogen evolution reaction, ACS Appl. Mater. Interfaces 8 (28) (2016) 18132—18139.

[23] D. Sun, C. Chang, S. Li, L. Lin, Near-field electrospinning, Nano Lett. 6 (4) (2006) 839—842.

[24] A. Cisquella-Serra, M. Magnani, Á. Gual-Mosegui, S. Holmberg, M. Madou, M. Gamero-Castaño, Study of the electrostatic jet initiation in near-field electrospinning, J. Colloid Interface Sci. 543 (2019) 106—113.

[25] X.X. He, J. Zheng, G.F. Yu, M.H. You, M. Yu, X. Ning, Y.Z. Long, Near-field electrospinning: progress and applications, J. Phys. Chem. C 121 (16) (2017) 8663—8678.

[26] S. Liu, D.H. Reneker, Droplet-jet shape parameters predict electrospun polymer nanofiber diameter, Polymer 168 (2019) 155—158.

[27] L. Ferrer-argemi, A. Cisquella-serra, M. Madou, J. Lee, "Temperature-Dependent electrical and thermal conductivity of glassy carbon wires, 2018 17th IEEE Intersoc. Conf. Therm. Thermomech. Phenom. Electron. Syst. (2018) 1280—1288.

[28] L. Ferrer-Argemi, E.S. Aliabadi, A. Cisquella-Serra, A. Salazar, M. Madou, J. Lee, Size-dependent electrical and thermal conductivities of electro-mechanically-spun glassy carbon wires, Carbon 130 (2018) 87—93.

[29] J.Y. Huang, S. Chen, Z.F. Ren, G. Chen, M.S. Dresselhaus, Real-time observation of tubule formation from amorphous carbon nanowires under high-bias Joule heating, Nano Lett. 6 (8) (2006) 1699—1705.

[30] Y. Yao, K.K. Fu, S. Zhu, J. Dai, Y. Wang, G. Pastel, Y. Chen, T. Li, C. Wang, T. Li, L. Hu, Carbon welding by ultrafast Joule heating, Nano Lett. 16 (11) (2016) 7282—7289.

[31] A. Salazar, B. Cardenas-Benitez, B. Pramanick, M.J. Madou, S.O. Martinez-Chapa, Nanogap fabrication by Joule heating of electromechanically spun suspended carbon nanofibers, Carbon 115 (2017) 811—818.

[32] P.J.F. Harris, Fullerene-related structure of commercial glassy carbons, Philos. Mag. 84 (29) (2004) 3159—3167.

[33] P.J.F. Harris, Z. Liu, K. Suenaga, Imaging the atomic structure of activatedcarbon, J. Phys. Condens. Matter 20 (36) (2008).

[34] K. Jurkiewicz, S. Duber, H.E. Fischer, A. Burian, Modelling of glass-like carbon structure and its experimental verification by neutron and X-ray diffraction, J. Appl. Crystallogr. 50 (1) (2017) 36—48.

[35] R. Natu, M. Islam, J. Gilmore, R. Martinez-duarte, Journal of analytical and applied pyrolysis shrinkage of SU-8 microstructures during carbonization, J. Anal. Appl. Pyrolysis 131 (2018) 17—27. February.

[36] S.P. Garland, T.M. Murphy, T. Pan, Print-to-pattern dry film photoresist lithography, J. Micromech. Microeng. 24 (5) (2014).

[37] J. LaDou, Printed circuit board industry, Int. J. Hyg Environ. Health 209 (3) (2006) 211—219.

[38] L. Soukup, I. Gregora, L. Jastrabik, A. Koňáková, Raman spectra and electrical conductivity of glassy carbon, Mater. Sci. Eng. B 11 (1—4) (1992) 355—357.

[39] F. Völklein, H. Reith, T.W. Cornelius, M. Rauber, R. Neumann, The experimental investigation of thermal conductivity and the Wiedemann-Franz law for single metallic nanowires, Nanotechnology 20 (32) (2009).

[40] J. Lee, Z. Li, J.P. Reifenberg, S. Lee, R. Sinclair, M. Asheghi, K.E. Goodson, Thermal conductivity anisotropy and grain structure in Ge2Sb2Te5 films, J. Appl. Phys. 109 (8) (2011) 1—6.

[41] G. Vitali, M. Rossi, M.L. Terranova, V. Sessa, Laser-induced structural modifications of glassy carbon surfaces, J. Appl. Phys. 77 (9) (1995) 4307—4311.

[42] D. Davazoglou, A. Moutsakis, V. Valamontes, V. Psycharis, Tungsten oxide thin films chemically vapor deposited at low pressure by W(CO)6 pyrolysis, J. Electrochem. Soc. 144 (2) (1997) 595—599.

[43] R.U. Kirss, L. Meda, Chemical vapor deposition of tungsten oxide, Appl. Organomet. Chem. 12 (3) (1998) 155—160.

[44] X. Peng, A. Chen, Aligned TiO2 nanorod arrays synthesized by oxidizing titanium with acetone, J. Mater. Chem. 14 (16) (2004) 2542—2548.

[45] M.F. Daniel, B. Desbat, J.C. Lassegues, B. Gerand, M. Figlarz, Infrared and Raman study of WO3 tungsten trioxides and WO3xH2O tungsten trioxide hydrates, J. Solid State Chem. 67 (2) (1987) 235—247.

[46] C.I. Vargas-Consuelos, K. Seo, M. Camacho-López, O.A. Graeve, Correlation between particle size and Raman vibrations in WO3 powders, J. Phys. Chem. C

118 (18) (2014) 9531–9537.

[47] K. Thummavichai, L. Trimby, N. Wang, C.D. Wright, Y. Xia, Y. Zhu, Low temperature annealing improves the electrochromic and degradation behavior of tungsten oxide (WOx) thin films, J. Phys. Chem. C 121 (37) (2017) 20498–20506.

[48] C. Guo, Y. Liu, X. Ma, Y. Qian, L. Xu, Synthesis of tungsten carbide nanocrystal via a simple reductive reaction, Chem. Lett. 35 (11) (2006) 1210–1211.

[49] F.C. Nava Alonso, M.L. Zambrano Morales, A. Uribe Salas, J.E. Bedolla Becerril, Tungsten trioxide reduction-carburization with carbon monoxide-carbon dioxide mixtures: kinetics and thermodynamics, Int. J. Miner. Process. 20 (1–2) (1987) 137–151.

[50] K.M. Reddy, T.N. Rao, J. Joardar, Stability of nanostructured W-C phases during carburization of WO3, Mater. Chem. Phys. 128 (1–2) (2011) 121–126.